Available online at www.sciencedirect.com

jmr&t Journal of Materials Research and Technology

journal homepage: www.elsevier.com/locate/jmrt

Original Article

Multi-spectroscopic analysis of high temperature oxides formed on cobalt-chrome-molybdenum alloys

Elia Marin [a,b,c,*], *Alex Lanzutti* [c,**], *Alfredo Rondinella* [c], *Francesco Sordetti* [c], *Michele Magnan* [c], *Taigi Honma* [a,b], *Yumi Yoshida* [a], *Wenliang Zhu* [a], *Giuseppe Pezzotti* [a,d,e], *Lorenzo Fedrizzi* [c]

[a] *Ceramic Physics Laboratory, Kyoto Institute of Technology, Sakyo-ku, Matsugasaki, 606-8585 Kyoto, Japan*
[b] *Department of Dental Medicine, Graduate School of Medical Science, Kyoto Prefectural University of Medicine, Kamigyo-ku, Kyoto 602-8566, Japan*
[c] *Dipartimento Politecnico di Ingegneria e Architettura, University of Udine, 33100, Udine, Italy*
[d] *Department of Immunology, Graduate School of Medical Science, Kyoto Prefectural University of Medicine, Kamigyo-ku, Kyoto 602-8566, Japan*
[e] *The Center for Advanced Medical Engineering and Informatics, Osaka University, Yamadaoka, Suita, 565-0871 Osaka, Japan*

ARTICLE INFO

Article history:
Received 26 May 2022
Accepted 14 August 2022
Available online 23 August 2022

Keywords:
Spectroscopy
Microscopy
CoCrMo
Cobalt chrome molybdenum
High temperature oxidation

ABSTRACT

Thanks to their thermal stability, resistance to oxidation and mechanical strength, cobalt-chrome molybdenum alloys are considered an ideal alloy for high temperature applications. The surface oxide layer evolves as a function of time and temperature, changing its chemical structure and increasing its thickness from a few nanometers to various microns. Making use of various diffractographic and spectroscopic techniques, namely X-ray diffraction, X-ray photoelectron spectroscopy, Raman spectroscopy and glow-discharge optical emission spectroscopy, coupled with complementary analysis, this work gives new insights on the chemical bonding, crystallographic structure, thickness and elemental composition of the oxide layers as a function of both time and temperature of oxidation. Results show that the initial nanometric passive layer of Co_3O_4 evolves into a metastable, sub-micrometric $CoCrO_4$ structure and finally stabilizes into a micrometric Cr_2O_3 at the highest temperatures. This paper fills a fundamental gap in the understanding of the chemistry and stability of Cobalt-based alloys used for high temperature applications, such as in poppet or exhaust valves, aerospace components or hot gas turbines. Once calibrated, this innovative, complete surface characterization approach can be ideally extended to other metallic alloys.

* Corresponding author.
** Corresponding author.
E-mail addresses: elia-marin@kit.ac.jp (E. Marin), alex.lanzutti@uniud.it (A. Lanzutti).
https://doi.org/10.1016/j.jmrt.2022.08.071

1. Introduction

The first scientist to produce an alloy by mixing Cobalt and Chrome was Elwood Haynes, back at the beginning of the XX century [1]. Haynes objective was to produce a material "which would not only resist oxidation and other harmful influences, but would also possess valuable physical properties, which would render them fit for special services". In 1907 and 1908, Haynes made series of different, innovative alloys by combining cobalt and chromium with tungsten and molybdenum, and then adding other elements such as zirconium, tantalum, thorium, titanium, vanadium, carbon, silicon and boron.

As he expected, his discoveries were able to resist for long time in extremely aggressive environments, as for example in boiling nitric acid, without even exhibiting signs of tarnishing [2].

One group of alloys in particular soon gained great scientific and industrial interest: trademarked by Union Carbide, Stellite Division under the name "Stellite" [3], these alloys found application in various fields where high wear-resistance was needed including aerospace industry [4], cutlery [5], bearings [6], blades [7], etc.

Despite displaying an array of impressive technological properties industrial uses of cobalt chrome alloys have been somehow limited to a niche of specific applications, mainly because of their costs [8], their limited machinability [9] and the impressive specific weight [10].

Cobalt-chrome alloys started to receive more attention when their true potential for biomedical applications was discovered, in the late 1950s. The use of stellite for orthopedic applications, in particular to repair bone fractures, has been actually proposed by Adalbert Zierold back in the 1920s [11], soon followed by the studies of Albert W. Merrick on Vitallium as a substitute for gold dental implants [12] and by the Vitallium femoral head resurfacing proposed by Smith-Petersen [12]. But it is not until the femoral prosthesis developed by Frederick R. Thompson, in the late 1950s, that the potential of cobalt-chrome as a structural biomaterial was fully understood [13].

The development of new cobalt chrome alloys over the years has been somehow limited: about 50 alloys are commonly used in industry today, still chemically quite similar to their ancestors developed more than one century ago, in particular for the biomedical field [14].

Despite their high technological importance, the understanding of the structure and evolution of cobalt chrome surface oxides is still somehow limited. When testing the Haynes 25 alloy high temperature tribological properties, Scharf et al. [6] reported the formation of a (Co,Cr),O layer, but were unable to identify which specific phase was formed. Some further insights were provided by Milošev and Strehblow using XPS and electrochemistry [15], who concluded that *"The alloy passivates spontaneously in air resulting in the formation of a thin oxide film containing mainly Cr_2O_3, with a minor contribution from Co- and Mo-oxides"*. By using XPS on oxygen io bombarded CoCrMo, Badovinac et al. [16] were able to observe the formation of CoO, Cr_2O_3, MoO_2, MoO_3, Mo_2O_5 $CoMoO_4$, showing that the chemical structure of the surface oxides of CoCrMo alloys are more complex than previously reported.

The number of technological fields in which these alloys are used, such as biomedical, sensor technology or heterogeneous catalysis [17–19], is constantly growing, but despite this, the study of their surface chemistry and oxide formation is still very limited [16].

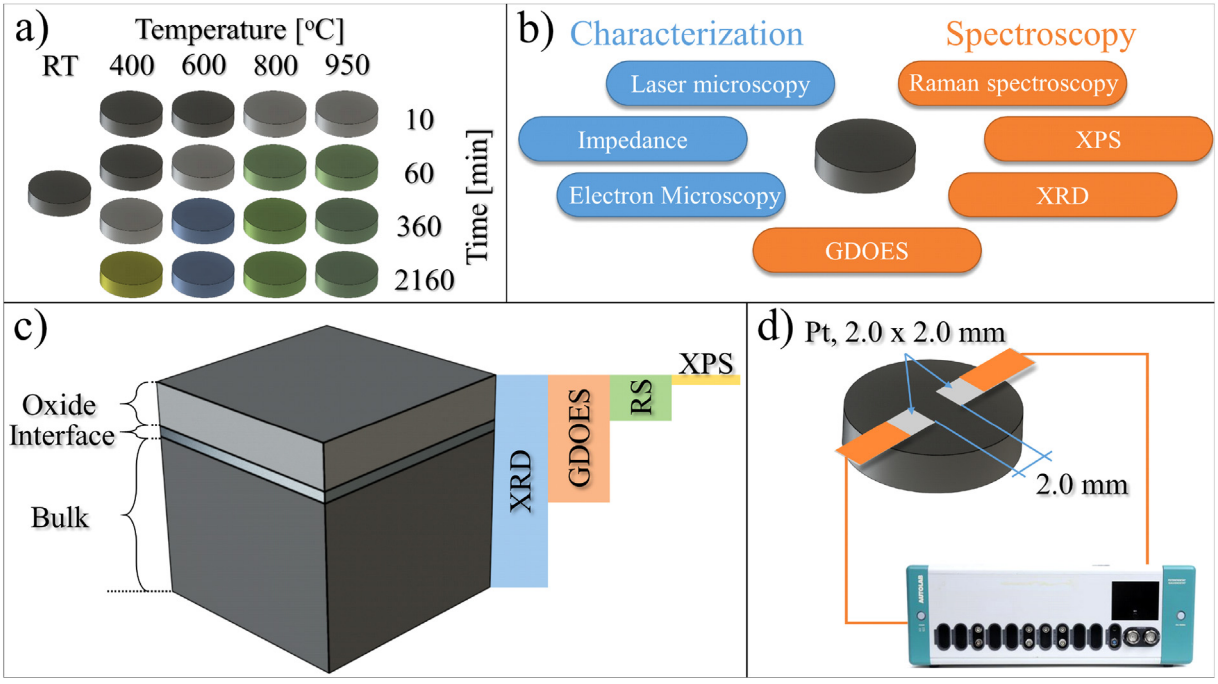

Fig. 1 – Schematic of the research: (a) thermal oxidation parameters (time and temperature), (b) list of experimental techniques, (c) schematic representation of the probe depth for each different spectroscopic technique and (d) schematic of the impedance testing.

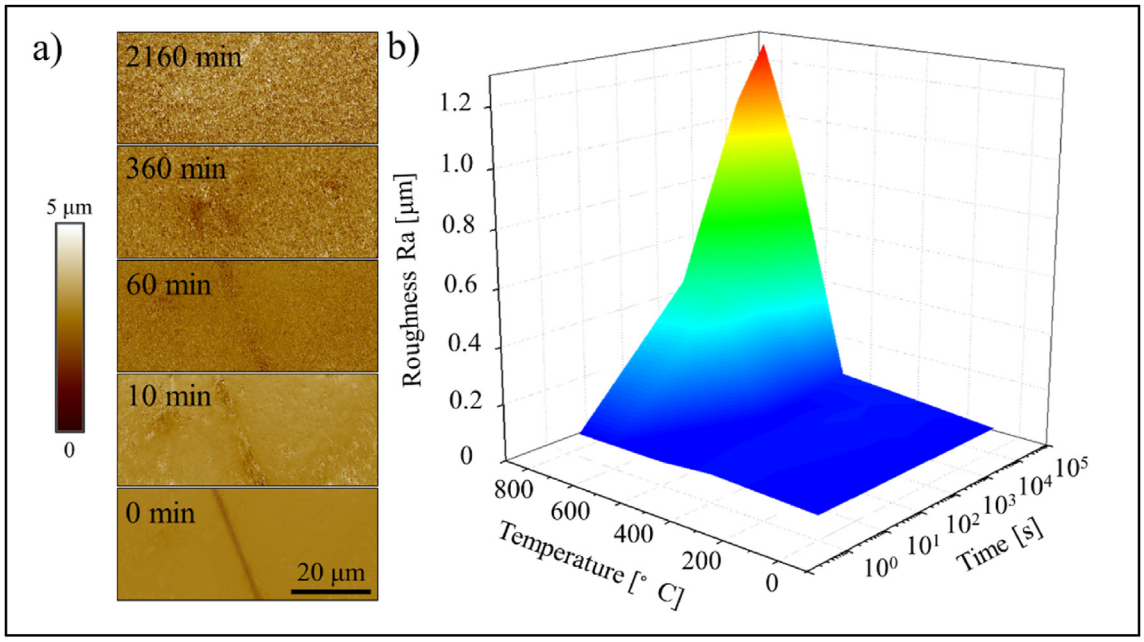

Fig. 2 – Surface morphology and roughness for the different samples. (a) evolution of the surface morphology for samples treated at 950 °C (same area in each image) and (b) surface Ra roughness as a function of time and temperature.

This study can help understand the mechanisms of oxide formation and how each metal affects the other within the alloy. This, in turn, can help improve the performance and increase the life-span of devices built with these alloys [15,20–25].

The objective of this research is to build up on previous literature results [26] by using a combination of four different spectroscopic techniques, namely X-ray diffraction (XRD), Glow Discharge Optical Emission Spectroscopy (GDOES), Raman spectroscopy (RS) and X-ray Photoelectron Spectroscopy (XPS), together capable of providing a high-resolution chemical and structural characterization of the surface oxides.

Between the metallic alloys of industrial interest, CoCrMo represent an ideal candidate for this pilot study as most oxide phases consisting of Co, Cr and Mo are Raman active, with a

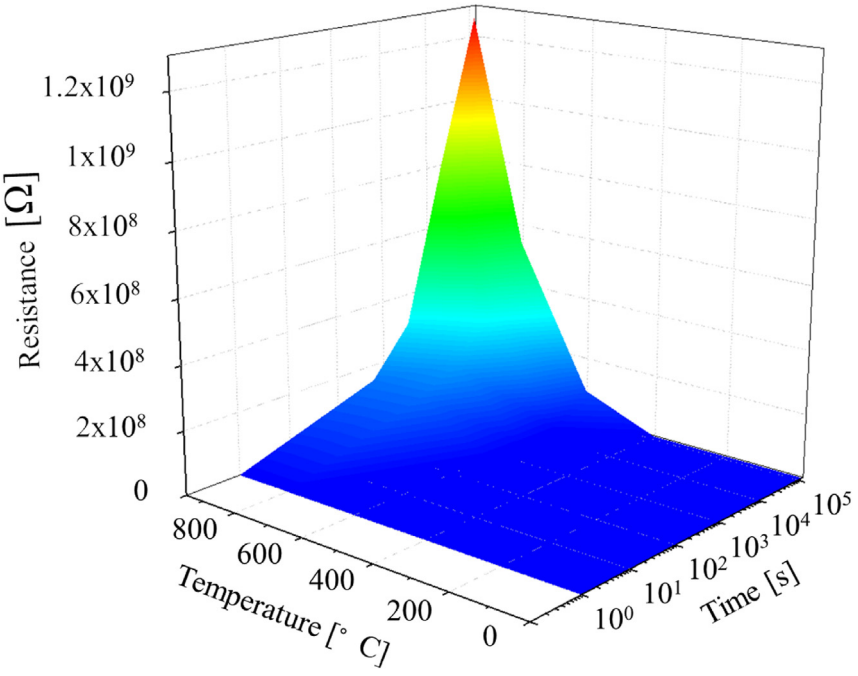

Fig. 3 – Electrical resistance as a function of time and temperature. As measured between the two platinum electrodes as configured in Fig. 1(d), as a function of temperature and time.

high relative intensity. The contents of this research and the experimental procedures are summarized in Fig. 1.

2. Results

Fig. 2(a) shows the surface morphology of the samples treated at 950 °C, at all-time intervals. The polished pristine surface becomes coarser with increasing treatment times. After 60 min of treatment, the marker scratch at the center of the image (with an initial depth of about 2 μm) is barely visible and it completely disappears after 360 min due to the formation of a thick oxide layer.

Samples treated at the two lowest temperatures (400 °C and 600 °C) maintain their surface morphologies up to 2160 min of thermal treatment, while for the intermediate temperature of 800 °C the roughness started to increase after about 10 min of treatment.

Fig. 2(b) shows the arithmetical average surface roughness (Ra) as measured after thermal treatment. It can be observed that roughness values are independent from temperature and time up to 600 °C and 2160 min of treatment, but then sharply increase after 10 min of treatment at higher temperatures. These results indicate that a possible temperature threshold for rapid surface deterioration (arbitrarily defined as an increase of one order of magnitude in Ra in 10 min or less) might be located between 600 and 800 °C.

Fig. 3 shows the electrical impedance measured on the sample surfaces as a function of temperature and time of treatment. It can be observed that, as expected, the graph trend is comparable with that of the surface roughness (Fig. 2) and thus oxide thickness, but with an important difference: unlike roughness, impedance already starts to rise at 600 °C and 60 min of treatment. These results suggest that chemical changes, oxygen diffusion in particular, are already happening in the oxide layer even without noticeable variations in roughness.

Samples cross section after 2160 min of treatment are resumed in Fig. 4.

The micrographs clearly show the presence of an oxide layer (above the dotted white line) in samples tested at 600 °C, 800 °C and 950 °C. The oxide seems to be composed by Cr and Co, although this signal is not so clearly visible in the map. The role of Mo is also not clear from these micrographs, due to the relatively low intensity. Further insights on the presence and role of Mo will be discussed along with the spectroscopic results.

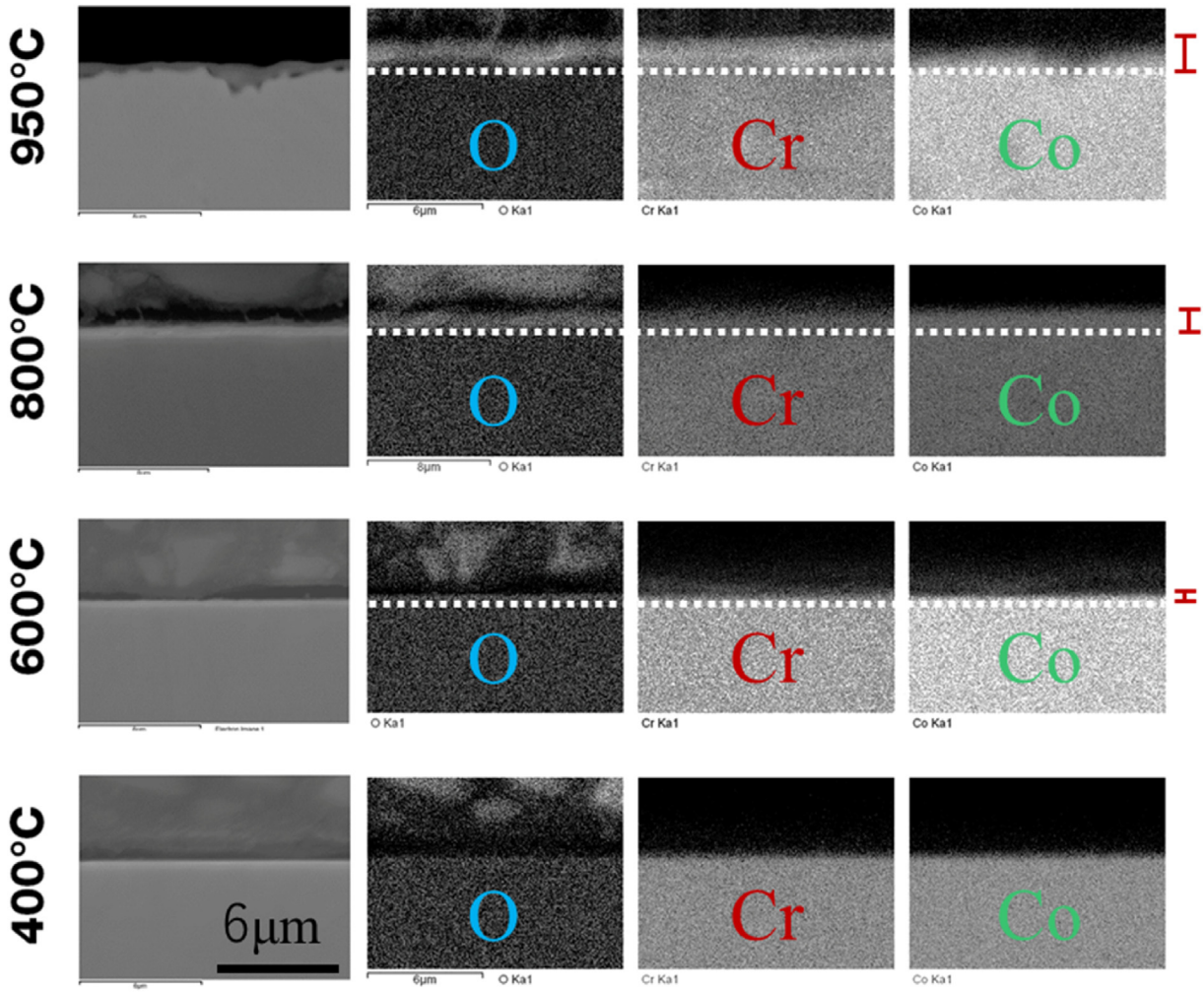

Fig. 4 – Cross sections and compositional analyses. SEM cross sections and EDXS maps for O, Cr and Co as obtained on the cross sectioned samples tested at 400 °C, 600 °C, 800 °C, 950 °C after 2160 min of treatment.

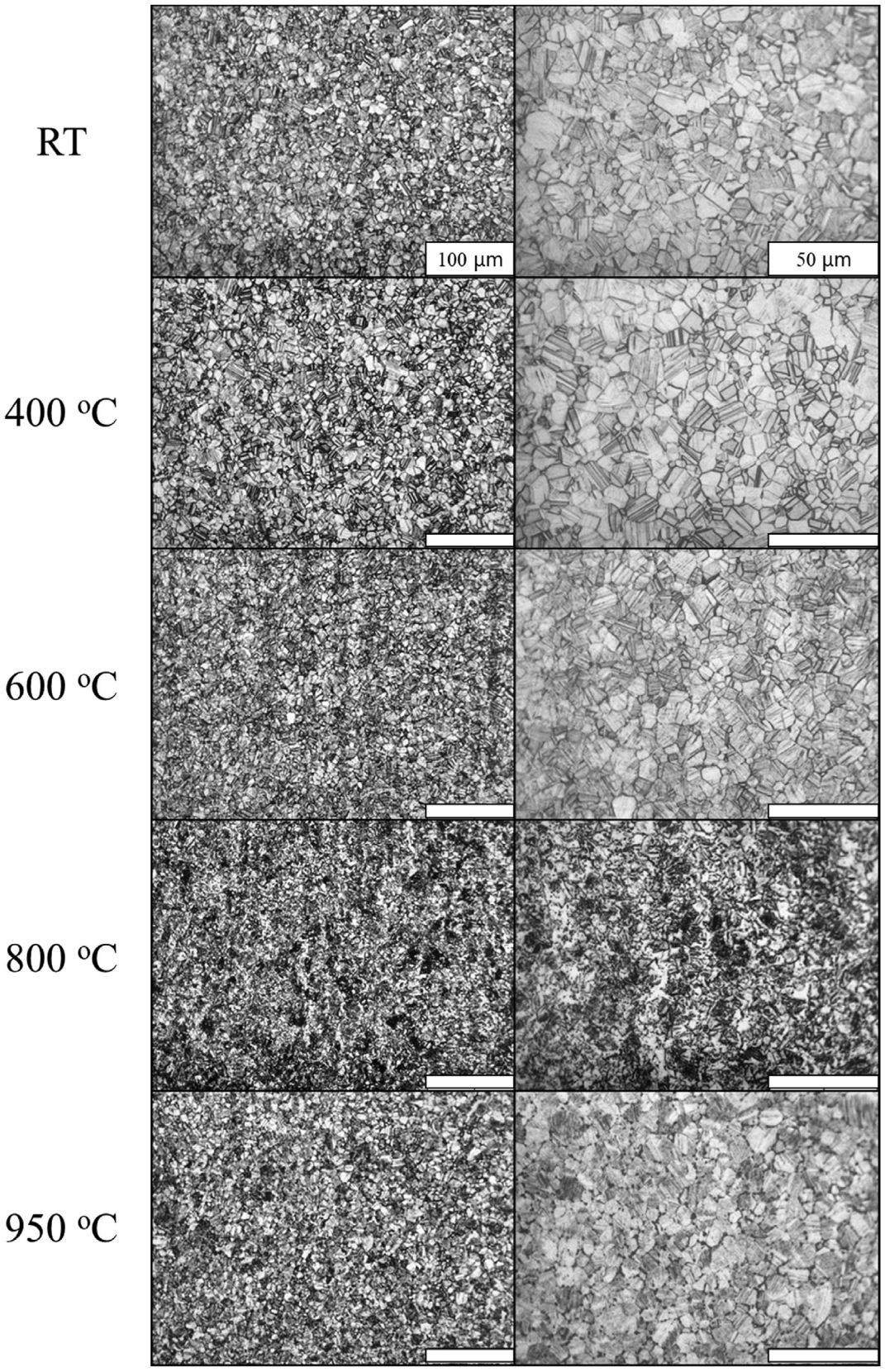

Fig. 5 – Microstructural observation of the samples cross sections. Presented as a function of temperature, after 2160 min of thermal treatment.

Light microscope analyses of the underneath material were performed in order to determine possible microstructural evolution of material during the oxidation tests, as presented in Fig. 5.

The microstructure is stable, under oxidation conditions, up to 600 °C. At 800 °C the microstructure decomposes and forms an additional phase that is the σ phase, richer in Cr respect the other phases. At 800 °C this phase if finer and randomly distributed in the material, while at 900 °C this phase becomes coarser and preferential displaced at grain boundaries.

The X-ray diffraction patterns obtained on the different samples after thermal treatment for 2160 min are resumed in Fig. 6. Both the pristine reference and the sample treated at 400 °C appear to be formed by two phases: a face-centered cubic structure (FCC), γ, and a hexagonal close-packed structure (HCP), ε [28]. The martensitic transformation γ → ε is usually the result of a fast cooling process, such as in the case of air cooling. The XRD measurements are confirmed by the microstructural characterization previously presented.

New peaks related to Cr_2O_3 (*) and $CoCr_2O_4$ (°) [29] and $Co_{0.8}Cr_{0.2}$ (§) [30]]start to appear when the temperature is raised to 600 °C, $CoCr_2O_4$ being the strongest secondary phase signal.

At 800 °C, peaks related to the hexagonal ε structure are no more visible on the diffraction pattern, while the peaks related to $CoCr_2O_4$ and $Co_{0.8}Cr_{0.2}$ reach the maximum intensity. The Cr_2O_3 signal also increase in intensity, and secondary peaks start to appear in the region between 20 and 40 2θ.

At 950 °C the peaks related to the Cr_2O_3 reach the maximum intensity, but bands associated with the face-centered cubic structure γ also reappear.

Raman imaging maps could be acquired on the same locations by using a grid of Vickers indentation as a marker. The results are shown in Fig. 7 as a function of both time and temperature. Cobalt chrome alloys are naturally protected from corrosion by a spontaneously formed layer of mixed oxides [15]. The layer itself is initially too thin to be detected by Raman spectroscopy, but even at temperature as low as 400 °C bands related to oxides can be detected on the Raman spectrum.

In Fig. 7, the red signal is related to the band located at 560 cm^{-1} produced by Cr_2O_3 [31], while the green signal is related to the band located at 690 cm^{-1} and produced by $CoCrO_4$ [32]. It can be observed that the results obtained after 2160 min of thermal treatment are in line with the diffraction patterns presented in Fig. 6, and in particular Cr_2O_3 can be predominantly observed at high temperature, while $CoCr_2O_4$ is stable at lower temperatures.

It is interesting to observe that the sample treated at 800 °C has an inhomogeneous distribution, with both regions at high Cr_2O_3 or at high $CoCr_2O_4$ content, the two apparently being mutually exclusive.

When treated at 950 °C for long time spans, the surface of the cobalt alloy starts to delaminate, resulting in the exposure of the underlying material, which appears green in Fig. 7, meaning that those regions are preferentially covered by $CoCr_2O_4$.

The average Raman spectra as a function of both time and temperature are presented in Fig. 8. Different phases are marked by using colored bars, green for Co_3O_4 [33], red for Cr_2O_3 [31] and blue for the intermediate $CoCr_2O_4$ [32]. For each phase, the spectral deconvolution is resumed in Table I.

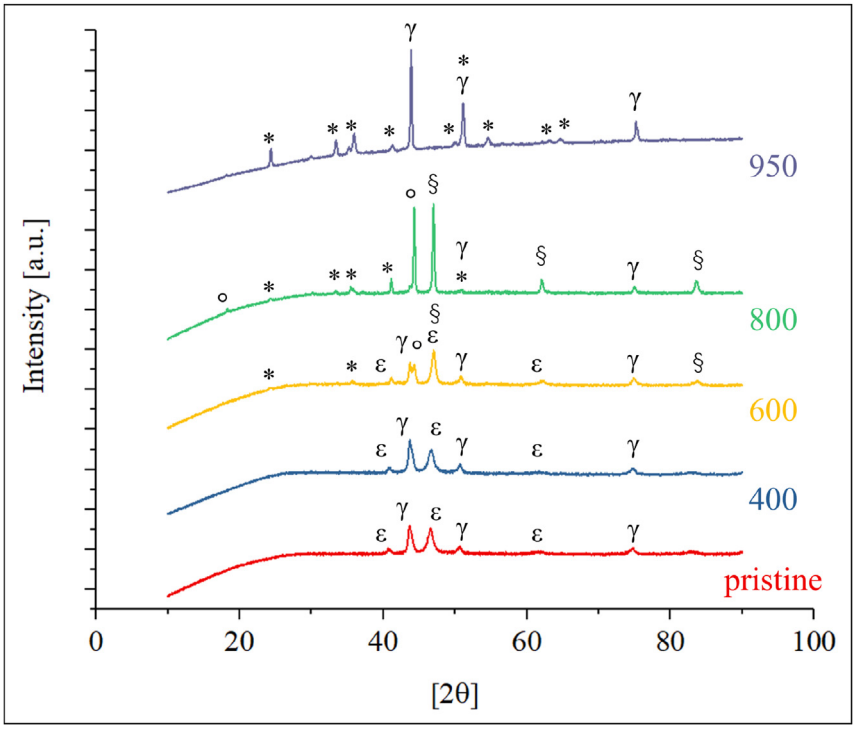

Fig. 6 – XRD diffraction patterns for the different samples. Presented as a function of temperatures and acquired at the longest time (2160 min), as compared to the pristine reference.

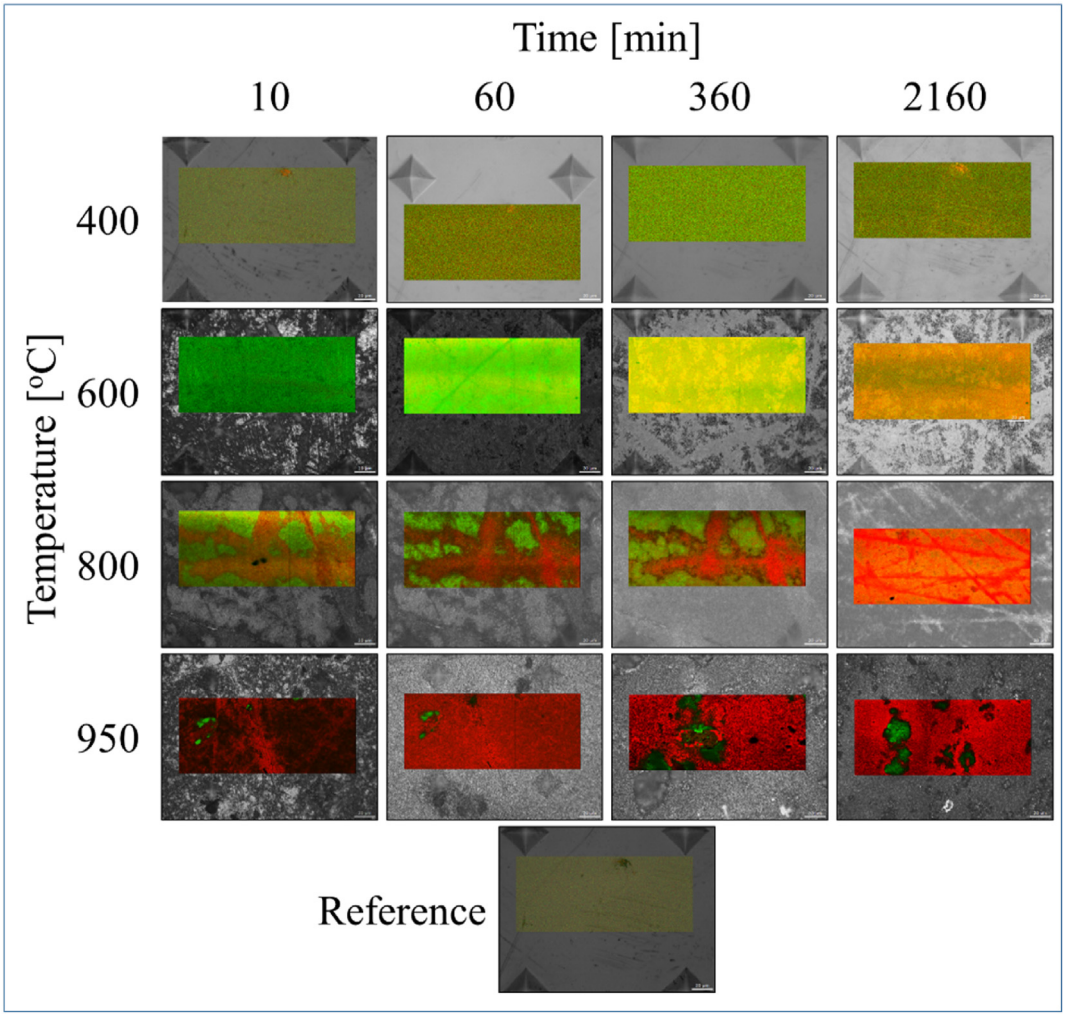

Fig. 7 – Raman imaging maps. As obtained at different heat treatment time steps on the same region of specimen treated at 400, 600, 800 and 950 °C. Red color for Cr_2O_3 and Green for $CoCrO_4$.

Due to the Fermi's sea of electrons effect, no Raman signal was expected to appear on the untreated samples [34]. Still, the Raman spectra of the pristine sample features a list of Raman bands at specific locations: 300 cm^{-1}, 680 cm^{-1}, 760 cm^{-1}, 995 cm^{-1}, 1400 cm^{-1}, 1740 cm^{-1}, 2125 cm^{-1} and 2250 cm^{-1}. A possible interpretation for some of these unexpected and not previously reported bands will be discussed in more detail the next chapter.

At the lowest treatment temperatures, Raman peaks are mainly related to the presence of Co_3O_4, and the intensity seems to increase with increasing the treatment time. At temperatures of 600 °C and 800 °C, after 10 min of treatment another phase appears, identified as $CoCr_2O_4$. Unlike Co_3O_4, $CoCr_2O_4$ appears to be metastable and disappears for longer treatment time in favor of the more thermodynamically stable Cr_2O_3.

At a temperature of 950 °C, a stable, relatively thick layer of Cr_2O_3 appears after only 10 min of treatment, with a relative intensity comparable to 360 min of treatment at 850 °C.

Further insights on the microstructure of the surface oxide layers were obtained by XPS. Fig. 9(a–c) shows the bands related to Oxygen, Chrome and Cobalt, respectively, as a function of the treatment temperature, for a thermal treatment time of 2160 min. The amount of O–H bonds on the surface of the samples is about constant and independent from the treatment temperature, as hydroxides are spontaneously formed on the surface of the alloy as a consequence of the exposure to humid air. M–O bonds, on the other hand, increase moving from the pristine material to the thermal treated specimen.

Surface chrome is initially present in two different forms: as metallic chrome and as Cr(III) (as in Cr_2O_3). After thermal treatment, the metallic chrome is reduced to zero, while the amount of Cr(III) increases to a value which appears to be independent from the treatment temperature [35,36].

As for chrome, cobalt is also initially present in two forms, metallic and Co(III) [35,36] and, as the metallic form disappears with thermal treatment, it is substituted by Co(II) [35,36], confirming the interpretation of the spectra obtained by Raman spectroscopy and XRD and related to the presence of $CoCr_2O_4$. The total amount of cobalt at the samples surface

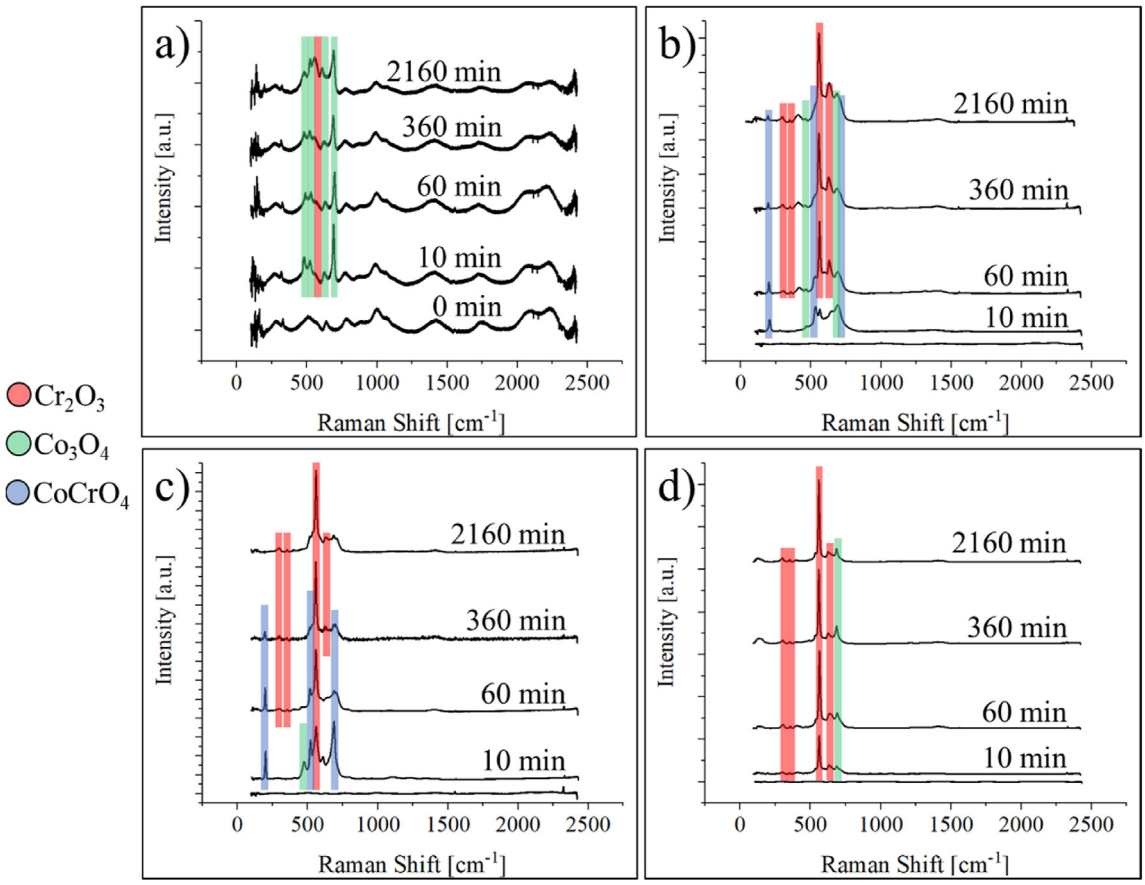

Fig. 8 – Average Raman spectra acquired on the surface of the samples. Results are presented as a function of time and temperature. Red color for Cr_2O_3, green for Co_3O_4 and blue for $CoCrO_4$. (a) treatment at 400 °C, (b) treatment at 600 °C, (c) treatment at 800 °C, (d) treatment at 950 °C.

seems to reach a maximum for a treatment temperature of 400 °C and decreases for higher temperature, to the point of being undetectable after treatments at 950 °C.

Unlike XRD, Raman Spectroscopy and XPS, by calibrating intensity signals and the rate of Argon sputtering GDOES can be used to obtain an in-depth compositional profile of the alloys. Results for samples treated for 2160 min are presented in Fig. 10. In his pristine conditions, the CoCrMo alloy possesses a slightly higher concentration of oxygen and cobalt on its outer surface, at the expenses of molybdenum. After treatment at 400 °C, the concentration of chrome and molybdenum increase for a few nanometers, at the expenses of cobalt. This layer is then followed by a thicker cobalt-enriched phase. Increasing the temperature to 600 °C leads to the formation of a superficial chrome oxide layer with a thickness of around 150 nm, followed by a cobalt-enriched layer with a thickness of about 300 nm. Further increases in temperature result in an increase the thickness of the chrome oxide layer, preventing the formation of the sub-superficial cobalt enriched layer.

The microhardness results obtained on the oxidized samples are shown in Fig. 11. It is observed an increase of hardness at the increase of the oxidation temperature, and thus to the oxide thickness. The main differences are observed for samples tested above 600 °C.

Table 1 – Assignation of the main Raman bands appearing in Fig. 8

Position [cm^{-1}]	Assignment	Phase	Reference
482		Co_3O_4	[33]
522		Co_3O_4	[33]
618		Co_3O_4	[33]
691		Co_3O_4	[33]
305	Eg	Cr_2O_3	[31]
360	Eg	Cr_2O_3	[31]
530	Eg	Cr_2O_3	[31]
560	A1g	Cr_2O_3	[31]
620	Fg	Cr_2O_3	[31]
195	F2g	$CoCr_2O_4$	[32]
460	E2g	$CoCr_2O_4$	[32]
517	F2g	$CoCr_2O_4$	[32]
685	A1g	$CoCr_2O_4$	[32]

3. Discussion

New insights on the composition of the surface oxides formed by thermal treatment on CoCrMo alloys could be acquired by combining together four different spectroscopic techniques.

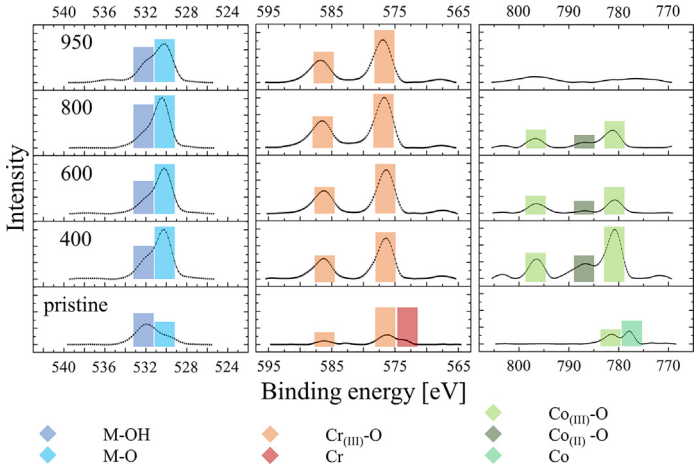

Fig. 9 – XPS results obtained on the samples treated at different temperatures for 2160min. Blue for Oxygen, orange for Chromium and green for Cobalt.

Three main phases could be identified: Co_3O_4, $CoCr_2O_4$ and Cr_2O_3, each one showing a different range of thermal stability, $CoCr_2O_4$ being the intermediate phase between the other two. In-depth compositional profiles acquired by GDOES (Fig. 10) clearly showed that the results obtained by all other techniques are actually the result of the superimposition of various stacked layers of oxides with different compositions.

Additionally, Raman spectroscopy results showed that, at a treatment temperature of 800 °C, two different stoichiometries of oxides are simultaneously formed on the surface of the samples, depending on the location.

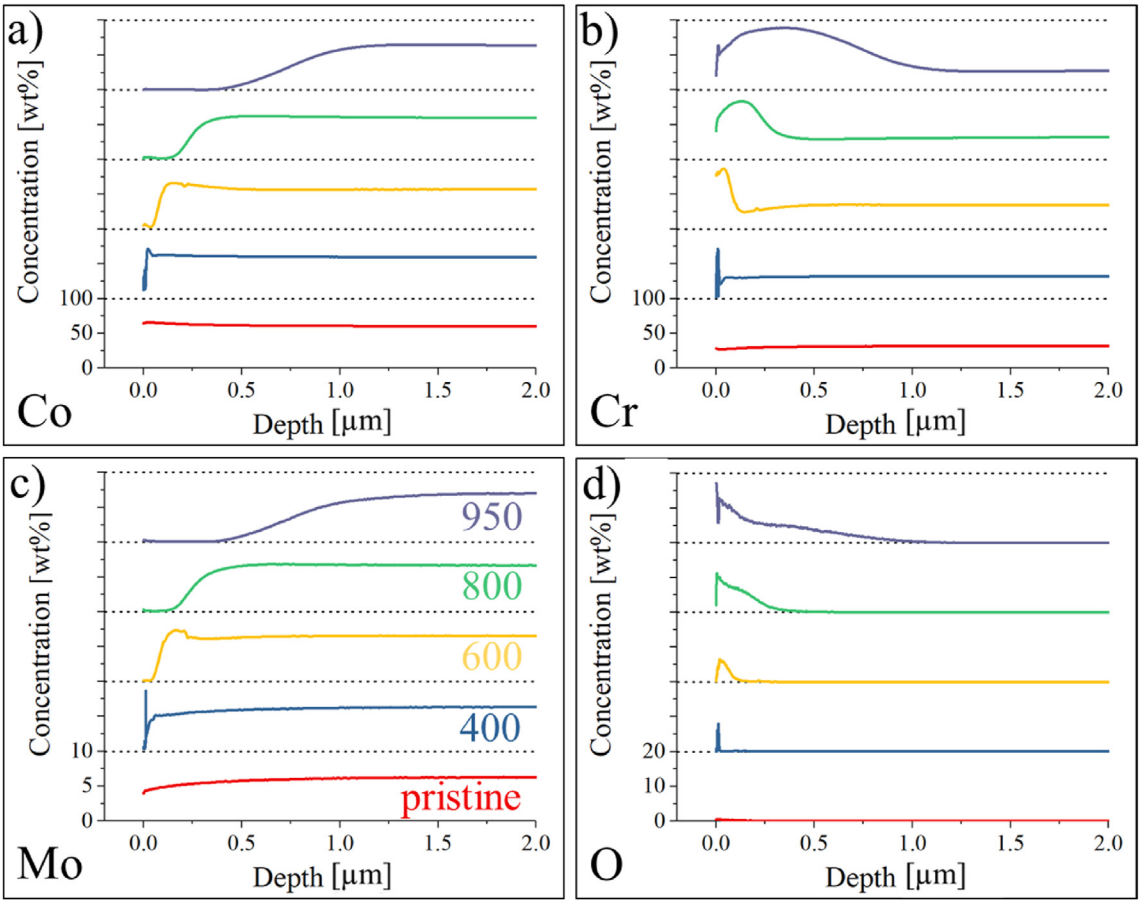

Fig. 10 – GDOES profiles of the four main elements as a function of temperature, for time of thermal treatment of 2160min. (a) cobalt, (b) chromium, (c) molybdenum, (d) oxygen.

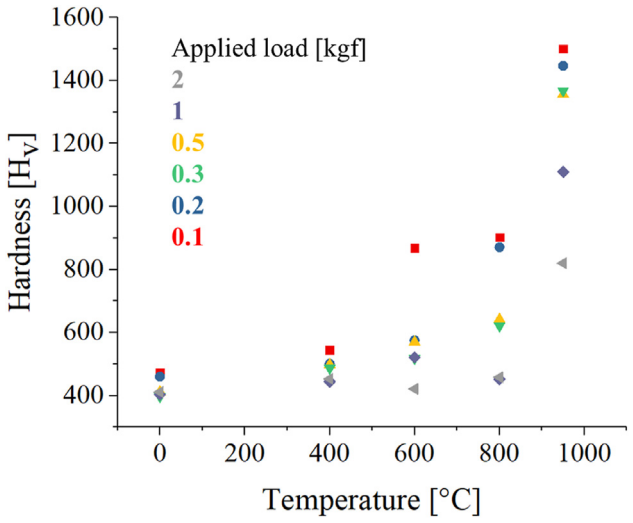

Fig. 11 – Microhardness results obtained on samples treated for 2160 min at different temperatures.

To better understand the oxide stratification, Fig. 12 shows the ratio between the signal of molybdenum (a) and cobalt (b) respect to the signal of chrome, and molybdenum respect to cobalt (c).

At each treatment temperature, the peak intensity of the Mo/Cr ratio (a) is more shallow with respect to the peak intensity of the Co/Cr ratio (b), meaning that two different phases, one containing relatively higher amounts of molybdenum and one containing relatively higher amounts of cobalt, can be found at different sputtering depths.

By considering the ratio between the molybdenum and the cobalt (c) and the signal of chrome and oxygen (Fig. 10(b) and (d)), a total of up to four different layers can be observed, at 950 °C: an initial spike in chrome and molybdenum (from 0 to a few nm), followed by chrome oxide (up to about 1 μm), then a cobalt enriched layer with lower levels of oxide (up to about 4 μm) and finally the bulk. Additionally, the lower ratio values up to about 300 nm in Fig. 12 (c) suggest that the solubility of cobalt in Cr_2O_3 is higher with respect to molybdenum.

At 400 and 600 °C, the GDOES signal of cobalt has a subsuperficial peak, which appears to be sharper at lower temperatures. The peak is caused by the presence of Co_3O_4, as evidenced both by Raman spectroscopy (Fig. 8(a)) and XPS (Fig. 9).

The molybdenum peaks visible on the GDOES spectrum of the sample treated at 400 °C give some possible insights on the interpretation of the unknown Raman bands in Fig. 8(a): Mo(II) oxides [37] or even more complex phases containing both chrome and molybdenum [38] can be responsible for the

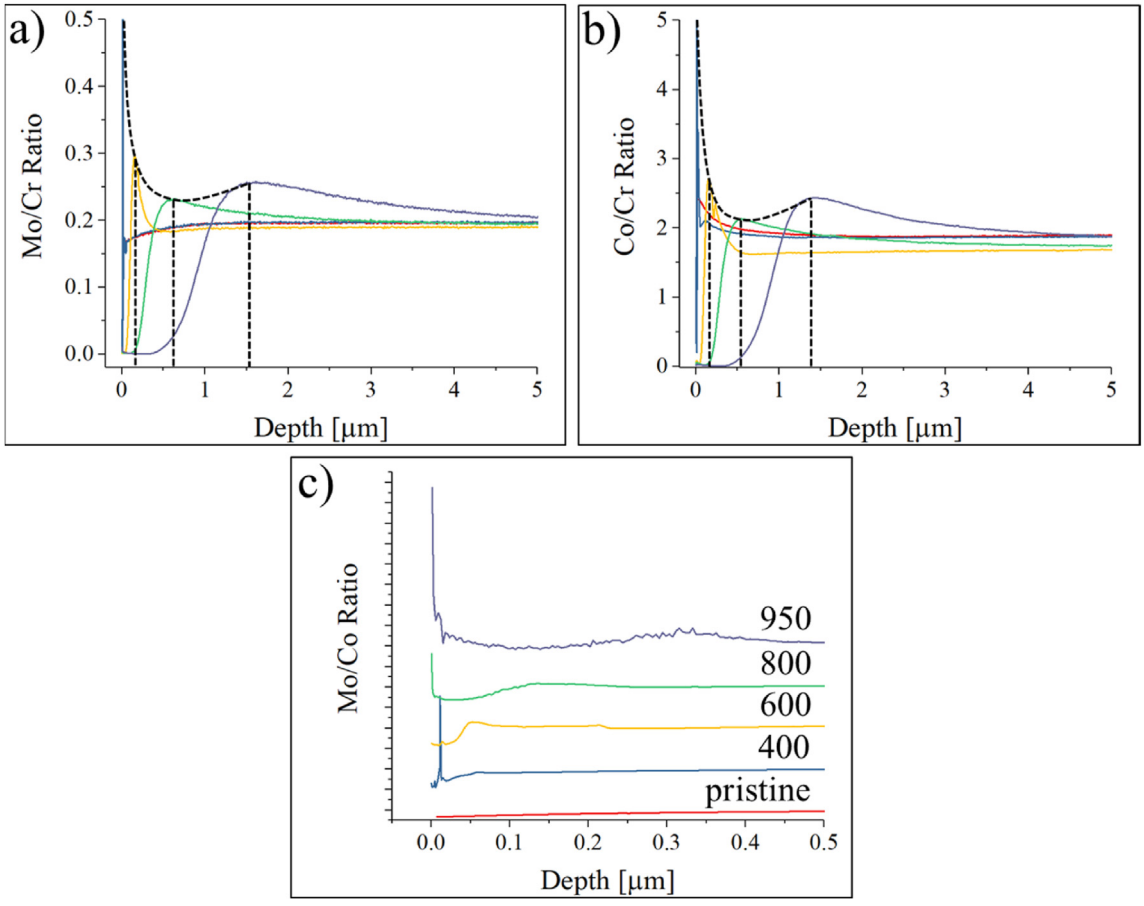

Fig. 12 – Relationship between the elements amount as a function of depth, for each temperature. (a) molybdenum over chromium, (b) cobalt over chromium and (c) molybdenum over cobalt.

bands located at about 800 and 1000 cm^{-1}. As the relative intensity of these phases is usually quite low, they can only be observed when the thickness of the surface oxide layer is low, before other, more intense bands appear.

4. Conclusions

Various diffractographic and spectroscopic techniques were combined in order to investigate the composition and structure of the oxides formed after thermal treatment of CoCrMo alloys.

Three main phases were identified: Co_3O_4, stable at lower treatment temperatures, Cr_2O_3, stable at higher temperatures and the intermediate $CoCr_2O_4$ phase.

GDOES results proved that the three phases can coexist in form of stratified layers, with Cr_2O_3 being the one exposed to the external environment and the Co-rich phases lying underneath.

A forth potential phase has been identified as a molybdenum or a chromium-molybdenum oxide, but its presence could only be detected by Raman spectroscopy or as a nanometric spike in the GDOES profiles.

Using Raman imaging, the contemporary growth of Cr and Co-rich oxides could be observed at intermediate treatment temperatures, following a preferential distribution potentially associated with the underlying metallographic structure.

5. Experimental procedures

5.1. Resource availability

5.1.1. Lead contact

Further information and requests for resources and reagents should be directed to and will be fulfilled by the lead contact, Elia Marin (elia-marin@kit.ac.jp).

5.1.2. Materials availability

All protocols describing the synthesis of the materials used in this research are provided in the manuscript.

5.1.3. Data and code availability

The authors declare that the data supporting the findings of this study are available within the paper. The authors declare that there was no code generated during the study.

5.2. Materials

ASTM F75 Cobalt Chrome Molybdenum discs (diameter 14 mm, thickness 3 mm) were obtained from an industrial producer (Sandvik, Stockholm, Sweden). Discs were then treated at different temperatures (0, 400, 600, 800 and 950 °C) for different time intervals (10, 60, 360, 2160 min), as also briefly summarized in Fig. 1. The initial surface roughness of the specimen was 25 nm Ra. Before testing and thermal treatments the samples were washed in ethanol using an ultrasonic bath.

5.3. Characterization

5.3.1. Laser microscopy

A VKX200K series laser microscope (Keyence, Osaka, Japan) was used to obtain low magnification images of large areas of the samples. The instrument could obtain both optical and topographical information on the surface morphology, with magnifications ranging from 10 × to 150 × and a numerical aperture between 0.30 and 0.95. The stage positioning could be controlled using by two step motors, while the autofocus function controlled the distance between the lenses and the surface of the sample, in the z range, allowing to perform automated focus stacking.

5.3.2. Electrical impedance

Electrical impedance measurements were performed using a AUTOLAB PGSTAT12 (Metrohm, Herisau, Switzerland) with a frequency response analyzer. The system consisted of two squared platinum electrodes (2 × 2 mm) at a constant distance of 2 mm that were pressed against the oxidized surface. The measurement was repeated at various randomized locations to obtain a statistically significant value.

5.3.3. Scanning electron microscopy

High magnification images of the samples cross section were acquired by using a EVO-40 (Carl Zeiss, Jena, Germany) with an acceleration voltage of 20 kV, a probe current of 5 nA, and operating at a fixed working distance of 10 mm. Before observation, the samples were cut using a low speed diamond blade and polished until obtaining a surface roughness of about 15 nm.

5.3.4. X-ray diffraction

XRD analyses were performed on a Rigaku Miniflex 60 system (Rigaku Corporation, Tokyo, Japan). The data were recorded at 30 mA and 40 kV generator settings, using Cu Kα radiation (λ = 0.154178 nm). Diffraction spectra were acquired in the range between 10° and 80° with a step size of 0.0158 at a rate of 1.5 s/step. The diffraction patterns were then matched with the ICCD/ICSD database after applying elemental database restrictions.

5.3.5. Raman imaging

Raman imaging was obtained using a dedicated Raman microscope coupled with a spectrometer (RAMANtouch, Nanophoton Co., Ltd., Osaka, Japan). The excitation source was a green light with a wavelength of 532 nm, produced by a diode laser. The instrument operated at a maximum nominal power of 200 mW. The power was set to an appropriate value by preliminary adjustment of neutral density filter. The microprobe used lenses ranging from 5x to 100x magnifications with numerical apertures from to 0.5 to 0.23.

5.3.6. Glow discharge optical emission spectroscopy

Glow discharge optical emission spectroscopy (GDOES) in-depth compositional profiles were acquired using a Horiba Jobin Yvon Rf-GD-profiler (Horiba Ltd., Kyoto, Japan). The instrument was equipped with a standard 4-mm-diameter anode and a poly-chromator equipped 28 different channels,

an Rf generator (13.6 MHz), and controlled by a Quantum XP software. Quantitative composition profiles were obtained with a calibration procedure using certified reference materials in order to estimate oxide thickness and composition.

5.3.7. *X-ray photoelectron spectroscopy*

XPS experiments were carried out using a photoelectron spectrometer (JPS-9010 MC; JEOL Ltd., Tokyo, Japan) with a MgK X-ray monochromatic source (output 10 kV, 10 mA). All measurements were conducted in a vacuum chamber at a pressure of about 1.5×10^{-7} Pa, upon setting the analyser pass energy to 10 eV and the voltage step size to 0.1 eV. For all samples, a wide scan was performed before acquiring 10 scan repetitions on each investigated region and specifically: Cobalt (Co2p, 785 eV), Chrome (Cr2p, 580 eV), Molybdenum (Mo3d, 232 eV) and Oxygen (O1s, 530 eV). The X-ray angle of incidence and the take-off angle were 34° and 90°, respectively.

5.3.8. *Light microscope analysis*

The samples, tested for 1 h at different temperatures, were cross sectioned with a refrigerated abrasive wheel, embedded in epoxy resin, grinded with water refrigerated SiC abrasive papers and finally polished with fabric discs and diamond suspension to obtain a mirror like surface. The samples were then etched, with a procedure described in other papers [35], and then the microstructure was analysed by light microscope underneath the high temperature oxide, to observe possible microstructural alterations of material due to both oxidative process and thermal effect on material.

5.3.9. *Microindentations*

Micro-hardness measurements at several loads (1.0 N, 2.0 N, 3 N, 4.9 N, 9.81 N and 19.6 N) were performed on samples' heat treated for 1 h in top view in order to determine the mechanical properties of the oxide, by using a procedure typical of thin films [27].

5.4. *Statistical significance*

For statistical purposes, all spectra have been acquired in 3 different locations on 3 different samples ($n = 9$). Statistical significance has been addressed by two-way ANOVA analysis of variance. Where possible, statistically significant results ($p < 0.05$) have been marked with an "*".

Author contributions

Conceptualization, E.M., A.L.; methodology, E.M., A.L.; investigation, E.M., A.L., A.R., T.H., M.M., F.S., Y.Y.; validation, W.Z.; formal analysis, W.Z.; resources, Y.Y., G.P., L.F.; funding acquisition E.M.; supervision, G.P., L.F., writing-original draft, E.M.; writing – review & editing, A.L., A.R.

Declaration of Competing Interest

The authors declare that they have no known competing financial interests or personal relationships that could have appeared to influence the work reported in this paper. The authors declare no competing interests.

REFERENCES

[1] Haynes E. Alloys of cobalt with chromium and other metals. J Ind Eng Chem 1913;5:189–91.
[2] Haynes, E. Metal alloy. Patent.
[3] Eastman J W Stellite. A history of the Haynes stellite company, 1912-1972. By ralph D. Gray. Kokomo, ind., stellite division, cabot corporation. Bus Hist Rev 1975;49(112):272–3.
[4] Freche JC, Ashbrook RL, Sandrock GD. High-temperature cobalt-tungsten alloys for aerospace applications. SAE Technical Paper Series; 1964. https://doi.org/10.4271/640501.
[5] Hawkins M. Why we need cobalt. B Appl Earth Sci 2001;110:66–70.
[6] Scharf TW, Prasad SV, Kotula PG, Michael JR, Robino CV. Elevated temperature tribology of cobalt and tantalum-based alloys. Wear 2015;330–331:199–208.
[7] Mann BS, Arya V. HVOF coating and surface treatment for enhancing droplet erosion resistance of steam turbine blades. Wear 2003;254:652–67.
[8] Campbell GA. The cobalt market revisited. Mineral Economics 2020;33:21–8.
[9] Zaman HA, Sharif S, Kim DW, Idris MH, Suhaimi MA, Tumurkhuyag Z. Machinability of cobalt-based and cobalt chromium molybdenum alloys - a review. Procedia Manuf 2017;11:563–70.
[10] Aherwar A, Singh AK, Patnaik A. Cobalt based alloy: a better choice biomaterial for hip implants. Trends Biomater Artif Organs 2016;30.
[11] Konstantinos M, Georgios K, Konstantinos S, Georgios T. The evolution of the surgical treatment of sports injuries in the 20th century: a historical perspective. Surg. Innov. 2016;23:538–42.
[12] Saadat E, Tiberi JV, Burke DW, Kwon Y-M. Smith-petersen Vitallium mold arthroplasty: case report with a fifty-one-year follow-up and histopathologic analysis. JBJS Case Connect 2013;3:e112.
[13] Hernigou P, Quiennec S, Guissou I. Hip hemiarthroplasty: from venable and bohlman to moore and thompson. Int Orthop 2014;38:655–61.
[14] Klarstrom D, Crook P, Mridha S. Cobalt alloys and designation system. In: Reference Module in materials science and materials Engineering. Elsevier; 2018.
[15] Milošev I, Strehblow H-H. The composition of the surface passive film formed on CoCrMo alloy in simulated physiological solution. Electrochim Acta 2003;48:2767–74.
[16] Jelovica Badovinac I, Kavre Piltaver I, Peter R, Saric I, Petravic M. Formation of oxides on CoCrMo surfaces at room temperature: an XPS study. Appl Surf Sci 2019;471:475–81.
[17] Hurt C, Brandt M, Priya SS, Bhatelia T, Patel J, Selvakannan PR, et al. Combining additive manufacturing and catalysis: a review. Catal Sci Technol 2017;7:3421–39. https://doi.org/10.1039/C7CY00615B.
[18] Hedberg YS, Qian B, Shen Z, Virtanen S, Wallinder IO. In vitro biocompatibility of CoCrMo dental alloys fabricated by selective laser melting. Dent Mater 2014;30:525–34. https://doi.org/10.1016/j.dental.2014.02.008.
[19] Mu D, Shen B, Zhao X. Effects of boronizing on mechanical and dry-sliding wear properties of CoCrMo alloy. Mater Des 2010;31:3933–6. https://doi.org/10.1016/j.matdes.2010.03.024.
[20] Schutze M. Materials science and technology: corrosion and environmental degradation. Weinheim: Wiley-VHC; 2000.

[21] Türkan U, Öztürk O, Eroğlu AE. Metal ion release from TiN coated CoCrMo orthopedic implant material. Surf. Coat. Tech. 2006;200:5020–7. https://doi.org/10.1016/j.surfcoat.2005.05.005.
[22] Futamoto M, Hirayama Y, Honda Y, Kikukawa A, Tanahashi K, Ishikawa A. CoCr-alloy perpendicular magnetic recording media for high-density recording. J Magn Magn Mater 2001:281–8. https://doi.org/10.1016/S0304- 8853(01)00359-6.
[23] Taurino AM, Forleo A, Francioso L, Siciliano P, Stalder M, Nesper R. Synthesis, electrical characterization, and gas sensing properties of molybdenum oxide nanorods. Appl Phys Lett 2006;88:152111. https://doi.org/10.1063/1.2192571.
[24] Poizot P, Laruelle S, Grugeon S, Dupont L, Tarascon JM. Nano-sized transitionmetal oxides as negative-electrode materials for lithium-ion batteries. Nature 2000;407:496–9. https://doi.org/10.1038/35035045.
[25] Qi W, Chen S, Wu Y, Xie K. A chromium oxide coated nickel/yttria stabilized zirconia electrode with a heterojunction interface for use in electrochemical methane reforming. RSC Adv 2015;5:47599–608. https://doi.org/10.1039/c5ra01927c.
[26] Lanzutti A, Andreatta F, Rossi L, Di Benedetto P, Causero A, Magnan M, et al. Corrosion fatigue failure of a high carbon CoCrMo modular hip prosthesis: failure analysis and electrochemical study. Eng Fail Anal 2019;105:856–68.
[27] Marin E, Lanzutti A, Fedrizzi L. Tribological properties of nanometric atomic layer depositions applied on AISI 420 stainless steel. Tribology in Industry; Kragujevac 2013:35 208–216.
[28] Wang Z, Yan Y, Qiao L. Effect of deformed subsurface on the corrosion resistance of biomedical CoCrMo alloy in simulated physiological solution. J Mater Sci 2020;55:13351–62.
[29] Durrani SK, Hussain SZ, Saeed K, Khan Y, Arif M, Ahmed N. Hydrothermal synthesis and characterization of nanosized transition metal chromite spinels. Turk J Chem 2012;36:111–20.
[30] Majerič D, Lazić V, Majerič P, Marković A, Rudolf R. Investigation of CoCr dental alloy: example from a casting workflow standpoint. Crystals 2021;11:849.
[31] Shim S-H, Duffy TS, Jeanloz R, Yoo C-S, Iota V. Raman spectroscopy and x-ray diffraction of phase transitions inCr2O3to 61 GPa. Phys. Rev. B Condens. Matter Mater. Phys. 2004;69.
[32] Tian Z, Zhu C, Wang J, Xia Z, Liu Y, Yuan S. Size dependence of structure and magnetic properties of CoCr2O4 nanoparticles synthesized by hydrothermal technique. J Magn Magn Mater 2015;377:176–82.
[33] Hadjiev VG, Iliev MN, Vergilov IV. The Raman spectra of Co3O4. J Phys C Solid State Phys 1988;21:L199.
[34] Clarke DG, Strong SP, Chaikin PM, Chashechkina EI. The quantum-classical metal. Science 1998. https://doi.org/10.1126/science.279.5359.2071.
[35] Survilienė S, Jasulaitienė V, Češūnienė A, Lisowska-Oleksiak A. The use of XPS for study of the surface layers of Cr–Co alloy electrodeposited from Cr (III) formate–urea baths. Solid State Ionics 2008;179(1–6):222–7.
[36] Hanawa T, Hiromoto S, Asami K. Characterization of the surface oxide film of a Co–Cr–Mo alloy after being located in quasi-biological environments using XPS. Appl Surf Sci 2001;183(1–2):68–75.
[37] Velvarská R, Tišler Z, Raichlová V, Hidalgo-Herrador JM. Raman spectroscopy as molybdenum and tungsten content analysis tool for mesoporous silica and beta zeolite catalysts. Molecules 2020;25.
[38] Tian H, Wachs IE, Briand LE. Comparison of UV and visible Raman spectroscopy of bulk metal molybdate and metal vanadate catalysts. J Phys Chem B 2005;109:23491–9.